

# Strain-shear coupling in bilayer MoS<sub>2</sub>

Jae-Ung Lee<sup>1,\*</sup>, Sungjong Woo<sup>2,\*</sup>, Jaesung Park<sup>1</sup>, Hee Chul Park<sup>2,3</sup>, Young-Woo Son<sup>2, †</sup> and Hyeonsik Cheong<sup>1,†</sup>

<sup>1</sup> Department of Physics, Sogang University, Seoul 04107, Korea

<sup>2</sup> Korea Institute of for Advanced Study, Seoul 02455, Korea

<sup>3</sup> Center for Theoretical Physics of Complex Systems, Institute of Basic Science, Daejeon 34051, Korea

\* These authors contributed equally to this work.

† Correspondence and requests for materials should be addressed to Y.-W. S. (email: hand@kias.re.kr) and H. C. (email: hcheong@sogang.ac.kr).

## Abstract

Layered materials such as graphite and transition metal dichalcogenides have extremely anisotropic mechanical properties owing to orders of magnitude difference between in-plane and out-of-plane interatomic interaction strengths. Although effects of mechanical perturbations on either intra- or inter-layer interactions have been extensively investigated, mutual correlations between them have rarely been addressed. Here we show that layered materials have an inevitable coupling between in-plane uniaxial strain and interlayer shear. Because of this, the uniaxial in-plane strain induces an anomalous splitting of the degenerate interlayer shear phonon modes such that the split shear mode along the tensile strain is not softened but hardened contrary to the case of intralayer phonon modes. We confirm the effect by measuring Raman shifts of shear modes of bilayer MoS<sub>2</sub> under strain. Moreover, by analyzing the splitting, we obtain an unexplored off-diagonal elastic constant, demonstrating that Raman spectroscopy can determine almost all mechanical constants of layered materials.

## Introduction

Three-dimensional (3D) layered materials such as graphite and transition metal dichalcogenides (TMDs) are formed by weak van der Waals force between two-dimensional (2D) crystals whereas atoms within each 2D crystal are bound through a strong covalent bonding. A huge difference between in-plane and out-of-plane interatomic interaction strengths often result in extremely anisotropic mechanical properties of 3D layered systems. Since electronic and mechanical properties of multilayered 2D crystals critically depend on their interlayer interactions<sup>1-3</sup>, understanding the influence of the external mechanical perturbations on the interlayer as well as intralayer interaction is very important. Mechanical properties of a single layer 2D crystal can be understood by analyzing variations of high-frequency optical phonon modes with external mechanical perturbations<sup>4-12</sup>. Similarly, the effects of interlayer interactions on mechanical properties can be analyzed by probing the low-frequency interlayer shear and breathing modes<sup>13-17</sup>. Raman spectroscopy, an invaluable diagnostic tool for 2D crystals, have played an important role in measuring these modes for various layered materials such as graphene and TMDs<sup>13-28</sup>. For example, intralayer<sup>11,12</sup> and interlayer<sup>13-17</sup> elastic moduli as well as their variations due to rotational and translational stacking faults<sup>29,30</sup> can be obtained by examining the ultralow-frequency Raman spectrum of layered 2D materials. As introduced here, the effects of mechanical perturbations on physical properties related with either intra- or inter-layer interactions separately have been studied extensively whereas mutual interplay between them have rarely been studied.

In this study, we attempt to elucidate the overall effect of external mechanical strain on the interlayer and intralayer interactions as well as the coupling between them. We first analyze the effect of tensile strain on bilayer MoS<sub>2</sub> using the analytic linear elastic model.

Then, we perform first-principles calculations on elastic constants of bilayer MoS<sub>2</sub>, a prototypical TMD material. Both the analytic model and the first-principles calculations predict that a uniaxial external mechanical strain along in-plane direction indeed couples to interlayer shear, splitting the degenerate low energy shear phonon modes. This indicates relative sliding of two layers with an external strain along in-plane direction. Contrary to usual phonon softening under tensile strain, our calculations show that the softened shear mode in strained bilayer MoS<sub>2</sub> is perpendicular to the applied tensile strain direction and vice versa. Next, we confirm the predicted frequency shift and splitting of the shear modes of bilayer MoS<sub>2</sub> by carrying out ultralow-frequency Raman scattering measurements under uniaxial strain. From a careful analysis on the polarized Raman spectroscopy data on split shear phonon modes, we can measure the off-diagonal elastic constant of the bilayer system that has not yet been explored. Our results could therefore provide a way to measure a whole set of elastic constants of layered systems that characterize their mechanical properties completely.

## Results

**Coupling between uniaxial strain and shear.** The bilayer 2H-MoS<sub>2</sub> has a stacked trigonal prismatic structure with inversion and three-fold rotational symmetry (Fig. 1a and b). So, the compliance tensor of the system with  $D_{3d}$  symmetry in a matrix form<sup>31</sup> is given by

$$\begin{pmatrix} \varepsilon_1 \\ \varepsilon_2 \\ \varepsilon_3 \\ \varepsilon_4 \\ \varepsilon_5 \\ \varepsilon_6 \end{pmatrix} = \begin{pmatrix} 1/E_i & -\nu_i/E_i & -\nu_o/E_i & s_{14} & 0 & 0 \\ -\nu_i/E_i & 1/E_i & -\nu_o/E_i & -s_{14} & 0 & 0 \\ -\nu_o/E_i & -\nu_o/E_i & 1/E_o & 0 & 0 & 0 \\ s_{14} & -s_{14} & 0 & s_{44} & 0 & 0 \\ 0 & 0 & 0 & 0 & s_{44} & -2s_{14} \\ 0 & 0 & 0 & 0 & -2s_{14} & 2(1+\nu_i)/E_i \end{pmatrix} \begin{pmatrix} \sigma_1 \\ \sigma_2 \\ \sigma_3 \\ \sigma_4 \\ \sigma_5 \\ \sigma_6 \end{pmatrix}. \quad (1)$$

Here,  $E_{i(o)}$  is the in-plane (out-of-plane) Young's modulus,  $\nu_{i(o)}$  is the in-plane (out-of-plane)

Poisson's ratio, and the vector form of strain and stress are defined as  $\varepsilon_1 = \varepsilon_{xx}$ ,  $\varepsilon_2 = \varepsilon_{yy}$ ,

$\varepsilon_3 = \varepsilon_{zz}$ ,  $\varepsilon_4 = 2\varepsilon_{yz}$ ,  $\varepsilon_5 = 2\varepsilon_{xz}$ ,  $\varepsilon_6 = 2\varepsilon_{xy}$ ,  $\sigma_1 = \sigma_{xx}$ ,  $\sigma_2 = \sigma_{yy}$ ,  $\sigma_3 = \sigma_{zz}$ ,  $\sigma_4 = \sigma_{yz}$ ,  $\sigma_5 = \sigma_{xz}$ ,

and  $\sigma_6 = \sigma_{xy}$ . The tensor form of strain is further defined as  $\varepsilon_{ij} = 1/2(\partial u_i/\partial x_j + \partial u_j/\partial x_i)$

with  $u_i$  being the local displacement vector component, and the corresponding stress tensor is

$\sigma_{ij} = \partial F / \partial \varepsilon_{ij}$ , where  $F$  is the free energy of the system<sup>31</sup>. A constant uniaxial tensile stress  $\sigma$

along a direction at an angle  $\varphi$  from the  $x$  axis in Fig. 1a corresponds to a stress tensor with

components  $\sigma_1 = \sigma \cos^2 \varphi$ ,  $\sigma_2 = \sigma \sin^2 \varphi$ ,  $\sigma_6 = \sigma \cos \varphi \sin \varphi$ , and  $\sigma_3 = \sigma_4 = \sigma_5 = 0$ , using

rotational tensor transformation of  $\sigma_{ij}$ . From equation (1), we find that such a stress leads to

strain components  $\varepsilon_4 = s_{14}\sigma \sin(\pi/2 - 2\varphi)$  and  $\varepsilon_5 = s_{14}\sigma \cos(\pi/2 - 2\varphi)$ . These correspond

to lateral sliding of the upper layer with respect to the lower layer by  $\Delta \mathbf{r} = (\Delta x, \Delta y)$  with

$\Delta x = 2d_{\text{int}}\varepsilon_{xz} = d_{\text{int}}\varepsilon_5 = d_{\text{int}}s_{14}\sigma \cos(\pi/2 - 2\varphi)$  and

$\Delta y = 2d_{\text{int}}\varepsilon_{yz} = d_{\text{int}}\varepsilon_4 = d_{\text{int}}s_{14}\sigma \sin(\pi/2 - 2\varphi)$ . This implies that the uniaxial stress causes

lateral sliding of the upper layer with respect to the lower layer in the direction at an angle of

$-2\varphi$  from the positive  $y$  axis if  $s_{14} > 0$ . If  $s_{14} < 0$ , the direction of sliding is reversed toward the

angle  $-2\varphi$  from the negative  $y$  axis, which is  $\pi - 2\varphi$  from the positive  $y$  axis.

For a simple case of a constant uniaxial tensile stress  $\sigma$  along the  $x$ -direction ( $\varphi=0^\circ$ ) as shown in Fig. 1d,  $\sigma_1=\sigma$  and  $\sigma_2=\dots=\sigma_6=0$  which lead to an off-diagonal strain component  $\varepsilon_4=s_{14}\sigma$ . This indicates that the stress can induce a lateral sliding between the two layers given by  $\Delta y = d_{\text{int}}\varepsilon_4 = d_{\text{int}}s_{14}\sigma$ , where  $d_{\text{int}}$  is the interlayer distance.

**First-principles calculations of shear mode splitting.** Applying a tensile strain typically softens the phonons along the direction of the strain because the effective spring constant along it becomes weaker owing to the elongation of interatomic distances<sup>4,6-10,32</sup>. Such a trend is found in our first-principles calculations and other studies for the intralayer optical phonon modes of strained MoS<sub>2</sub><sup>7-10</sup>. For the intralayer  $E_g$  mode of bilayer MoS<sub>2</sub>, the calculated frequency shifts match our experiments very well and are found to be linear up to 2% strain (See Supplementary Fig. 1). However, opposite results are obtained for the interlayer shear modes. Figure 2 shows the calculated phonon frequency shift of the interlayer shear modes of the same system with respect to the uniaxial strain; the higher frequency mode ( $S^+$ ) corresponds to the vibrations along the strain axis, whereas the lower frequency mode ( $S^-$ ) corresponds to the vibrations perpendicular to it. Our first-principles calculations show that the shifts barely depend on the strain direction (See Fig. 2 and Supplementary Fig. 2). By inspecting the relaxed atomic structures for phonon calculation under strain, we have found that the two layers slide with respect to each other as uniaxial strain is applied. This indeed agrees with the aforementioned analysis of the compliance tensor of the system. The amount of strain-induced interlayer sliding based on the first-principles calculation is not negligible at all and is about a half percent of the lattice constant for the applied strain of one percent. It is also confirmed that the direction of sliding matches well with our model prediction.

We have found that the stress-induced layer sliding is the origin of the anomalous shear mode splitting. We first assume that the interlayer coupling for the shear modes is mainly determined by the interaction between adjacent sulfur atoms at the interface. These interface sulfur atoms also form a buckled hexagonal lattice, where each sublattice belongs to a different sulfur layer (Fig. 1d). Therefore, the splitting of shear modes would solely depend on the way of breaking the hexagonal symmetry in the hexagonal network between the nearest sulfur atoms at the interface between the top and bottom layers of bilayer MoS<sub>2</sub>. From the compliance tensor analysis explained earlier, the strain along the zigzag direction ( $\sigma_1 = \sigma$  and otherwise zero), for example, induces an interlayer shift along the armchair direction (Fig. 1d). Such a layer sliding along the armchair direction breaks the symmetry in the interface hexagonal lattice similar to the distorted intralayer hexagonal lattice under strain along the armchair direction (Fig. 1c). Thus, the effective bond distance between interface sulfur atoms parallel to the strain direction is shortened while the perpendicular one is elongated as schematically illustrated in Fig. 1. This is indeed opposite to the in-plane bond elongation within a single layer under the same strain. Thus, one can expect that the polarization dependence of Raman scattering intensity of the hardened shear mode should be similar to that of softened intralayer optical phonon modes and vice versa. From our first-principles calculations, we have also checked that the frequency splitting for the case of uniaxial stretching without sliding. It has shown that the splitting becomes ten times smaller compared to the splitting when the sliding is properly considered (See Supplementary Fig. 2). We developed a detailed interface phonon model using effective interatomic interaction between the sulfur atoms at the interface and obtain a quantitative expression for the splitting of shear phonon modes under strain agreeing well with our first-principles calculation results (Supplementary Note 1 and Supplementary Fig. 3). From all theoretical considerations, we

expect that the anomalous splitting of shear phonon modes under uniaxial strain should occur irrespective of direction of applied in-plane strain.

**Raman spectroscopic determination of shear mode splitting.** We have performed polarized Raman experiments to compare with our theoretical prediction. Bilayer MoS<sub>2</sub> samples are prepared directly on acrylic substrates by mechanical exfoliation from MoS<sub>2</sub> flakes (Supplementary Fig. 4). The number of layers is determined by combination of optical contrast, Raman and photoluminescence (PL) measurements. Experimental details of application of strain and polarized ultralow-frequency Raman measurements are presented in Methods section.

Figure 3a shows the Raman spectra of bilayer MoS<sub>2</sub> for different uniaxial strains up to 1.88%. The  $A_{1g}$  and  $E_g$  modes of bilayer MoS<sub>2</sub> correspond to intralayer vibrations, the interlayer in-plane mode (shear mode,  $S$ ) corresponding to  $E_g$  and the interlayer out-of-plane  $A_{1g}$  mode (breathing mode,  $B$ ) are also observed (See Supplementary Fig. 4a for schematics of vibration modes)<sup>14,15</sup>. First, we focus on the intralayer high frequency modes under strain. The in-plane  $E_g$  mode redshifts and splits into two peaks as the strain increases, whereas the  $A_{1g}$  mode does not vary much<sup>7-10</sup>. Since the  $A_{1g}$  mode is an out-of-plane mode, the effect of in-plane strain is minimal<sup>7-10</sup>. The  $E_g$  mode splits owing to the symmetry breaking of the hexagonal lattice<sup>4,7,10,32</sup>. We label the split mode with lower (higher) frequency as  $E_g^-$  ( $E_g^+$ ). We note that since the strain lowers symmetry of the system, the vibration modes of the strained MoS<sub>2</sub> are no longer  $E_g$ <sup>8,28</sup>. Nevertheless, we label the split modes as  $E_g^-$  and  $E_g^+$  in order to indicate their origin. The overall behavior of intralayer Raman modes of bilayer MoS<sub>2</sub> is similar to that of the single-layer case<sup>7,10</sup>. The interlayer shear ( $S$ ) and breathing ( $B$ )



modes show negligible dependence on strain. These results are summarized in Fig. 3b. Assuming linear dependence of the frequencies on the uniaxial strain, the shift rates of the  $E_g^-$ ,  $E_g^+$ , and  $A_{1g}$  modes for bilayer are obtained to be  $-4.0 \pm 0.1$ ,  $-0.9 \pm 0.2$ , and  $-0.3 \pm 0.1$   $\text{cm}^{-1}\%$ , respectively, agreeing well with previous studies<sup>7</sup>. We compared the experimental data with calculations with different in-plane Poisson's ratio (See Supplementary Fig. 1). The experimental results seem to fit best with calculations with the Poisson's ratio of intrinsic bilayer  $\text{MoS}_2$  ( $\nu_{\parallel}=0.22$ )<sup>33</sup>, which we used for the following analysis. From the shift rates, the Grüneisen parameter ( $\gamma$ ) and the shear deformation potential ( $\beta$ ) for the  $E_g$  modes are calculated as  $\gamma=1.0 \pm 0.2$  and  $\beta=0.8 \pm 0.2$ , which are also similar to previous results<sup>7</sup> (Supplementary Note 3). The polarization dependences of the in- and out-of-plane intralayer modes with strain are shown in Fig. 4a and summarized in Figs. 4b and c, respectively. By inspecting the polarized Raman spectrum of in-plane intralayer modes, we can determine the direction of strain with respect to the crystal orientation following the well-established procedure<sup>4</sup> (Supplementary Note 4). Analyzing the data in Fig. 4b, we obtain the crystallographic orientation of the sample,  $\varphi=15.7 \pm 1.1^\circ$ . For another sample, we obtained  $\varphi=23.8 \pm 2.1^\circ$  (Supplementary Fig. 5).

Now we turn our focus onto the interlayer shear modes. Figures 5a and b compare the polarization dependence of the low-frequency Raman modes without and with uniaxial strain, respectively. The intensity of the breathing mode ( $B$ ) shows a dependence on the polarization similar to the case of the  $A_{1g}$  mode irrespective of strain. Under strain, the shear mode peak intensity does not seem to depend on polarization, and no apparent splitting is observed at any given polarization. Upon close inspection, however, one can notice that the shear mode peak at  $\sim 22.8 \text{ cm}^{-1}$  seems to move periodically with polarization unlike the unstrained case as

shown in Figures 5a and b. Since the phonon mode frequency itself should not depend on polarization, the apparent polarization-dependent shift can only be interpreted as being due to polarization dependence of the relative intensities of closely spaced peaks due to strain-induced splitting. This kind of a small splitting can be distinguished with a help of polarization<sup>34,35</sup> because degeneracy-lifted phonon modes have different polarization dependences<sup>4,6,10,32</sup>. Since the peaks are not resolved well at any particular polarization angle, a simple double Lorentzian fitting of individual spectrum would not be able to determine the splitting reliably. Therefore, we measured a whole set of 37 spectra as a function of polarization at fixed strain of 1.28%. Since the frequency of the modes should not depend on the polarization, the whole set of 37 spectra were fitted as a whole by requiring that the peak positions are the same in all 37 spectra and only the relative intensities vary (Fig. 5c). By doing so, one can greatly reduce the experimental uncertainty in the positions of the two peaks as shown in Fig. 5c and find that the peak splitting is  $\sim 0.91 \pm 0.05 \text{ cm}^{-1}$  under 1.28% uniaxial strain. The validity of this procedure is ascertained by Fig. 5d, in which the intensities of the split peaks obtained through the fitting procedure follow the dependences expected from strain-split peaks of  $E_g$  phonon modes (Supplementary Note 4).

For the interlayer shear modes, we denote the low and high frequency modes as  $S^-$  and  $S^+$ , respectively, as mentioned earlier. The polarization dependence of the shear and breathing modes are shown in Figs. 5d and e. We also find almost similar shifts in other samples with different strain directions (Supplementary Fig. 5). The experimentally obtained peak positions under strain are plotted in Fig. 2, which show good agreement with our first-principles calculations. As expected from our theoretical analysis, the splitting behavior of the interlayer shear modes is indeed in sharp contrast to the intralayer case in that the split mode in the direction parallel to the uniaxial strain hardens while the other mode in the

direction perpendicular to it softens with strain. The polarization dependence of  $S^+$  (Fig. 5d) is the same as that of  $E_g^-$  (Fig. 4b), and vice versa, confirming our theoretical analysis. The corresponding Grüneisen parameter and shear deformation potentials for the interlayer shear phonon are obtained to be  $0.9 \pm 0.3$  and  $2.4 \pm 0.4$ , respectively.

## Discussion

An off-diagonal elastic modulus  $s_{14}$  can be obtained by comparing the experimental data with the model based on the interface hexagonal sulfur networks. With a simple spring model between the interface sulfur atoms, the amount of frequency splitting can be estimated to be  $\Delta\omega = (\omega_0 d_{\text{int}} \gamma' |s_{14}| E_i / 2k) \varepsilon$ , where  $\omega_0$ ,  $d_{\text{int}}$ ,  $E_i (= 1/s_{11})$ , and  $\varepsilon$  are the phonon frequency without strain, the interlayer distance, the in-plane Young's modulus, and the strain along the applied uniaxial stress, respectively;  $k$  is the lateral component of the effective spring constant between nearest-neighbor interface sulfur atoms from different layers;  $\gamma'$  is the linear scaling factor of  $k$  to the change of interatomic distance from the equilibrium; and  $s_{14}$  is the element of the compliance tensor between  $\varepsilon_1$  and  $\sigma_4$  (See Supplementary Note 1 for derivation of  $\Delta\omega$ ). On the other hand, the average shift  $\bar{\omega}$  of the two split frequencies is given by  $\Delta\bar{\omega} = \bar{\omega} - \omega_0 = -(1 - \nu_i)(\omega_0 \gamma' a_{\text{SS}} / 4k) \varepsilon$  (see Supplementary Note 1 for derivation), where  $a_{\text{SS}}$  is the interlayer sulfur-to-sulfur lateral distance, and  $\nu_i$  is the in-plane Poisson's ratio.

Combining the expressions for  $\Delta\omega$  and  $\Delta\bar{\omega}$ , we obtain

$|s_{14}| = -(a_{\text{SS}} / d_{\text{int}})((1 - \nu_i) / 2E_i) \Delta\omega / \Delta\bar{\omega}$ . With  $a_{\text{SS}} = 0.18$  nm,  $d_{\text{int}} = 0.62$  nm,  $\nu_i = 0.22$ ,  $E_i = 0.33$  TPa<sup>33,36,37</sup> and the experimental values of  $\Delta\omega/\varepsilon = 0.60 \pm 0.13$  cm<sup>-1</sup>%<sup>-1</sup>, and  $\Delta\bar{\omega}/\varepsilon = -0.15 \pm 0.04$  cm<sup>-1</sup>%<sup>-1</sup>, we find that  $|s_{14}|$  of MoS<sub>2</sub> is  $1.46 \pm 0.34$  TPa<sup>-1</sup>. Most of the uncertainty comes from

a small  $\Delta\bar{\omega}$  value that goes into the denominator. Within this uncertainty, our experimentally obtained  $|s_{14}|$  value is consistent with our first-principles calculation result of  $0.84 \text{ TPa}^{-1}$ , which is obtained following a procedure similar to that in Ref. 33. From these considerations, we tabulate all relevant elastic parameters in Table 1, and the complete matrix elements of compliance tensor in Eq. (1) for bilayer  $\text{MoS}_2$  can be written as

$$\begin{pmatrix} \varepsilon_1 \\ \varepsilon_2 \\ \varepsilon_3 \\ \varepsilon_4 \\ \varepsilon_5 \\ \varepsilon_6 \end{pmatrix} = \begin{pmatrix} 3.0 & -0.67 & -0.55 & -1.46 & 0 & 0 \\ -0.67 & 3.0 & -0.55 & 1.46 & 0 & 0 \\ -0.55 & -0.55 & 17 & 0 & 0 & 0 \\ -1.46 & 1.46 & 0 & 111 & 0 & 0 \\ 0 & 0 & 0 & 0 & 111 & 2.92 \\ 0 & 0 & 0 & 0 & 2.92 & 7.4 \end{pmatrix} \begin{pmatrix} \sigma_1 \\ \sigma_2 \\ \sigma_3 \\ \sigma_4 \\ \sigma_5 \\ \sigma_6 \end{pmatrix}, \quad (2)$$

where the matrix elements are in the unit of  $\text{TPa}^{-1}$ . Here, we used experimental values wherever available.

By analyzing the low frequency Raman spectrum, we have shown that the hitherto unexplored off-diagonal elastic constant  $s_{14}$  of  $\text{MoS}_2$  can be estimated. Our study here can be easily extended to other multilayered 2D crystals and could open a new way to determine almost all elastic constants of layered materials.

## Methods

**Computational Methods.** For the theoretical analysis, we have carried out first-principles calculations using Quantum ESPRESSO package<sup>38</sup> with plane wave basis and norm-conserving pseudopotentials<sup>39</sup>. To include the interlayer van der Waals interaction properly, we used the revised version<sup>40</sup> of the nonlocal correlation functional method developed by Vydrov and van Voorhis<sup>41</sup>. Phonon frequencies are calculated using density functional perturbation theory<sup>38,42</sup>. The energy cutoff for the basis set expansion is 110 Ry. Such a high

energy cutoff is adopted for resolving the low frequencies of interlayer shear modes which is order of a few meV. The  $k$ -point grid of  $8 \times 8 \times 1$  is used. In order to obtain  $s_{14}$ , we have alternatively calculated  $s_{56}$  ( $= -2s_{14}$ ) by inverting the matrix form of the shear part of stiffness tensor  $c_{ijkl}$ , where  $i, j, k, l = x, y, z$ . The stiffness tensor is defined by  $c_{ijkl} = \partial^2 F / \partial \varepsilon_{ij} \partial \varepsilon_{kl}$ . Here  $F$  is the total free energy of the system from the first-principles calculations as a function of discrete values of strain  $\varepsilon_{ij}$  up to 5 %, and the differentiation is done numerically. The thickness of a bilayer MoS<sub>2</sub> is set to be twice the interlayer distance. For more details, refer to Supplementary Note 2.

**Experimental details of Raman measurements.** The bilayer samples of MoS<sub>2</sub> were prepared directly on acrylic substrates by mechanical exfoliation from MoS<sub>2</sub> flakes (SPI supplies). The number of layers was determined by the combination of optical contrast, Raman and PL measurements (Supplementary Fig. 4). The uniaxial strain is applied by a four-probe bending stage and calculated by  $\varepsilon = t_0 \theta / L_0$ , where  $L_0$  and  $t_0$  is unstrained length and thickness of acrylic substrate,  $\theta$  is an angle in arc by bending substrate<sup>6-8</sup>. The laser beam was focused onto the sample by a 50× microscope objective lens (0.8 N.A.), and the scattered light was collected and collimated by the same objective. The scattered signal was dispersed with a Jobin-Yvon Triax 550 spectrometer (1800 grooves mm<sup>-1</sup>) and detected with a liquid-nitrogen-cooled back-illuminated charge-coupled-device (CCD) detector. To access the low-frequency range below 100 cm<sup>-1</sup>, reflective volume holographic filters (Ondax) were used to reject the Rayleigh-scattered light. The spectral resolution of our system is  $\sim 0.7$  cm<sup>-1</sup>. The laser power was kept below 0.2 mW in order to avoid heating.

**Data availability.** The data that support the findings of this study are available from the corresponding author upon request.

## References

1. Castro Neto, A. H., Guinea, F., Peres, N. M. R., Novoselov, K. S. & Geim, A. K. The electronic properties of graphene. *Rev. Mod. Phys.* **81**, 109–162 (2009).
2. Geim, A. K. & Grigorieva, I. V. Van der Waals heterostructures. *Nature* **499**, 419–425 (2013).
3. Zhang, X. *et al.* Phonon and Raman scattering of two-dimensional transition metal dichalcogenides from monolayer, multilayer to bulk material. *Chem. Soc. Rev.* **44**, 2757–2785 (2015).
4. Mohiuddin, T. M. G. *et al.* Uniaxial strain in graphene by Raman spectroscopy: *G* peak splitting, Grüneisen parameters, and sample orientation. *Phys. Rev. B* **79**, 205433 (2009).
5. Huang, M., Yan, H., Heinz, T. F. & Hone, J. Probing strain-induced electronic structure change in graphene by Raman spectroscopy. *Nano Lett.* **10**, 4074–9 (2010).
6. Yoon, D., Son, Y.-W. & Cheong, H. Strain-Dependent Splitting of the Double-Resonance Raman Scattering Band in Graphene. *Phys. Rev. Lett.* **106**, 155502 (2011).
7. Conley, H. J. *et al.* Bandgap Engineering of Strained Monolayer and Bilayer MoS<sub>2</sub>. *Nano Lett.* **13**, 3626–3630 (2013).
8. Zhu, C. R. *et al.* Strain tuning of optical emission energy and polarization in monolayer and bilayer MoS<sub>2</sub>. *Phys. Rev. B* **88**, 121301 (2013).

9. Rice, C. *et al.* Raman-scattering measurements and first-principles calculations of strain-induced phonon shifts in monolayer MoS<sub>2</sub>. *Phys. Rev. B* **87**, 81307 (2013).
10. Wang, Y., Cong, C., Qiu, C. & Yu, T. Raman Spectroscopy Study of Lattice Vibration and Crystallographic Orientation of Monolayer MoS<sub>2</sub> under Uniaxial Strain. *Small* **9**, 2857–2861 (2013).
11. Lee, J.-U., Yoon, D. & Cheong, H. Estimation of Young's Modulus of Graphene by Raman Spectroscopy. *Nano Lett.* **12**, 4444–4448 (2012).
12. Metten, D., Federspiel, F., Romeo, M. & Berciaud, S. All-Optical Blister Test of Suspended Graphene Using Micro-Raman Spectroscopy. *Phys. Rev. Appl.* **2**, 1–11 (2014).
13. Tan, P. H. *et al.* The shear mode of multilayer graphene. *Nat. Mater.* **11**, 294–300 (2012).
14. Zhao, Y. *et al.* Interlayer Breathing and Shear Modes in Few-Trilayer MoS<sub>2</sub> and WSe<sub>2</sub>. *Nano Lett.* **13**, 1007–1015 (2013).
15. Zhang, X. *et al.* Raman spectroscopy of shear and layer breathing modes in multilayer MoS<sub>2</sub>. *Phys. Rev. B* **87**, 115413 (2013).
16. Li, Y., Lin, S., Chui, Y. S. & Lau, S. P. Effect of Uniaxial Strain on Low Frequency Raman Modes in Few Layers Molybdenum Disulfide. *ECS J. Solid State Sci. Technol.* **5**, Q3033–Q3037 (2016).
17. Huang, S. *et al.* Low-Frequency Interlayer Raman Modes to Probe Interface of Twisted Bilayer MoS<sub>2</sub>. *Nano Lett.* **16**, 1435–1444 (2016).
18. Lee, J.-U., Park, J., Son, Y.-W. & Cheong, H. Anomalous excitonic resonance Raman effects in few-layered MoS<sub>2</sub>. *Nanoscale* **7**, 3229–3236 (2015).

19. Lee, J.-U. *et al.* Raman Signatures of Polytypism in Molybdenum Disulfide. *ACS Nano* **10**, 1948–1953 (2016).
20. Puretzy, A. A. *et al.* Low-Frequency Raman Fingerprints of Two-Dimensional Metal Dichalcogenide Layer Stacking Configurations. *ACS Nano* **9**, 6333–6342 (2015).
21. Lu, X. *et al.* Rapid and Nondestructive Identification of Polytypism and Stacking Sequences in Few-Layer Molybdenum Diselenide by Raman Spectroscopy. *Adv. Mater.* **27**, 4502–4508 (2015).
22. Lui, C. H., Ye, Z., Keiser, C., Xiao, X. & He, R. Temperature-activated layer-breathing vibrations in few-layer graphene. *Nano Lett.* **14**, 4615–4621 (2014).
23. Lui, C. H., Ye, Z., Keiser, C., Barros, E. B. & He, R. Stacking-dependent shear modes in trilayer graphene. *Appl. Phys. Lett.* **106**, 41904 (2015).
24. He, R. *et al.* Coupling and Stacking Order of ReS<sub>2</sub> Atomic Layers Revealed by Ultralow-Frequency Raman Spectroscopy. *Nano Lett.* **16**, 1404–1409 (2016).
25. Lorchat, E., Froehlicher, G. & Berciaud, S. Splitting of Interlayer Shear Modes and Photon Energy Dependent Anisotropic Raman Response in N -Layer ReSe<sub>2</sub> and ReS<sub>2</sub>. *ACS Nano* **10**, 2752–2760 (2016).
26. Qiao, X.-F. *et al.* Polytypism and unexpected strong interlayer coupling in two-dimensional layered ReS<sub>2</sub>. *Nanoscale* **8**, 8324–8332 (2016).
27. Zhao, H. *et al.* Interlayer interactions in anisotropic atomically thin rhenium diselenide. *Nano Res.* **8**, 3651–3661 (2015).
28. Chen, S., Goldstein, T., Venkataraman, D., Ramasubramaniam, A. & Yan, J. Activation of New Raman Modes by Inversion Symmetry Breaking in Type II Weyl Semimetal Candidate 1T'-MoTe<sub>2</sub>. *Nano Lett.* **16**, 5852–5860 (2016).



29. Wu, J.-B. *et al.* Resonant Raman spectroscopy of twisted multilayer graphene. *Nat. Commun.* **5**, 5309 (2014).
30. Wu, J.-B. *et al.* Interface Coupling in Twisted Multilayer Graphene by Resonant Raman Spectroscopy of Layer Breathing Modes. *ACS Nano* **9**, 7440–7449 (2015).
31. Nye, J. F. *Physical Properties of Crystals*. (Oxford University Press, 1985).
32. Huang, M. *et al.* Phonon softening and crystallographic orientation of strained graphene studied by Raman spectroscopy. *Proc. Natl. Acad. Sci.* **106**, 7304–7308 (2009).
33. Woo, S., Park, H. C. & Son, Y.-W. Poisson's ratio in layered two-dimensional crystals. *Phys. Rev. B* **93**, 75420 (2016).
34. Lee, J.-U. *et al.* Polarization dependence of double resonant Raman scattering band in bilayer graphene. *Carbon* **72**, 257–263 (2014).
35. Chen, S.-Y., Zheng, C., Fuhrer, M. S. & Yan, J. Helicity-Resolved Raman Scattering of MoS<sub>2</sub>, MoSe<sub>2</sub>, WS<sub>2</sub>, and WSe<sub>2</sub> Atomic Layers. *Nano Lett.* **15**, 2526–2532 (2015).
36. Castellanos-Gomez, A. *et al.* Elastic properties of freely suspended MoS<sub>2</sub> nanosheets. *Adv. Mater.* **24**, 772–775 (2012).
37. Geng, K., Yang, F. & Grulke, E. A. Nanoindentation of submicron polymeric coating systems. *Mater. Sci. Eng. A* **479**, 157–163 (2008).
38. Giannozzi, P. *et al.* QUANTUM ESPRESSO: a modular and open-source software project for quantum simulations of materials. *J. Phys. Condens. Matter* **21**, 395502 (2009).
39. Vanderbilt, D. Soft self-consistent pseudopotentials in a generalized eigenvalue formalism. *Phys. Rev. B* **41**, 7892–7895 (1990).

40. Sabatini, R., Gorni, T. & de Gironcoli, S. Nonlocal van der Waals density functional made simple and efficient. *Phys. Rev. B* **87**, 41108 (2013).
41. Vydrov, O. A. & Van Voorhis, T. Nonlocal van der Waals density functional: The simpler the better. *J. Chem. Phys.* **133**, 244103 (2010).
42. Baroni, S., De Gironcoli, S., Dal Corso, A. & Giannozzi, P. Phonons and related crystal properties from density-functional perturbation theory. *Rev. Mod. Phys.* **73**, 515–562 (2001).

### **Acknowledgements**

This work was supported by the National Research Foundation (NRF) grant funded by the Korean government (MSIP) (NRF-2016R1A2B3008363 and No. 2017R1A5A1014862, SRC program: vdWMRC center) and by a grant (No. 2011-0031630) from the Center for Advanced Soft Electronics under the Global Frontier Research Program of MSIP. Computations were supported by the Center for Advanced Computation of Korea Institute for Advanced Study.

### **Author contributions**

H. C. and Y.-W. S. supervised the project. S.W. and H. C. P. performed first-principles calculations and model analysis. J.-U. L. and J. P. performed Raman spectroscopy measurements and data analysis. Y.-W. S. and H. C. co-wrote the paper and J.-U. L. and S. W. commented on the manuscript. All authors discussed the results and manuscript at all stages.

**Additional information**

**Supplementary Information** accompanies this paper at <http://www.nature.com/>

naturecommunications

**Competing interests:** The authors declare no competing financial interests.

## Figures and captions

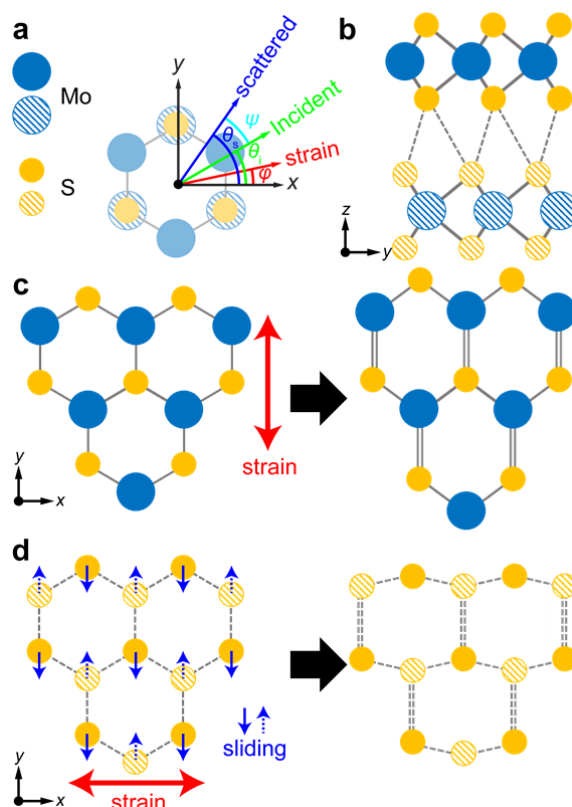


**Figure 1| Lattice structure of bilayer MoS<sub>2</sub> under uniaxial strain.** (a) Definitions of angles. (b) Side view of crystal structure of bilayer MoS<sub>2</sub>. The atoms in the top layer are shown as solid circles whereas those in the bottom layer are shown as hashed circles. (c) Top view of unstrained single-layer MoS<sub>2</sub> (left panel) and distorted lattice structure under armchair strain (right panel). Solid lines are for Mo-S covalent bonds. The double lines denote a longer bond distance compared to the single line. (d) Top view of hexagonal network of interface sulfur atoms in unstrained bilayer MoS<sub>2</sub> (left) and distorted lattice structure under zigzag strain (right). Sulfur atoms belonging to the upper (lower) layer are denoted by yellow filled (hashed) circles. The dotted lines indicate interlayer van der Waals bonds between interface sulfur atoms. Here, the double and single lines indicate the lengthened and shortened interfacial sulfur bond distances, respectively. Zigzag strain in single-layer MoS<sub>2</sub> and armchair strain in bilayer MoS<sub>2</sub> induce similar lattice distortions.

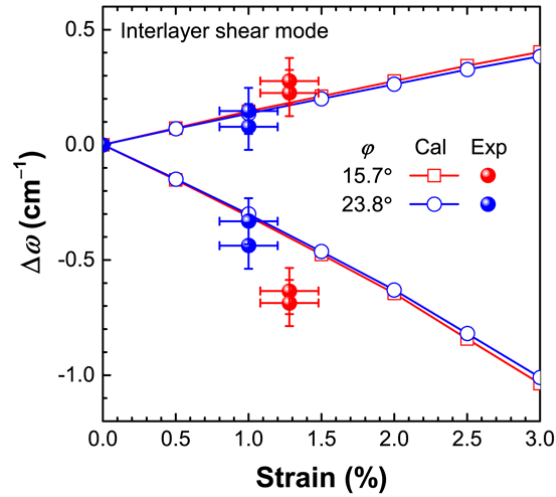


**Figure 2| Splitting of interlayer shear mode under uniaxial strain.** Shifts of split interlayer shear modes under uniaxial tensile strain for two different strain directions of  $\varphi=15.7^\circ$  (red) and  $23.8^\circ$  (blue). Calculation (open circle and square) and experimental (filled symbols) results are compared. For the experimental data, values obtained from the Stokes and anti-Stokes spectra are plotted. Experimental error bars in strain come from the uncertainty in the estimate of the strain using the equation  $\varepsilon=t_0\theta/L_0$ . The error bars in  $\Delta\omega$  are defined by the standard deviation of experimental values.

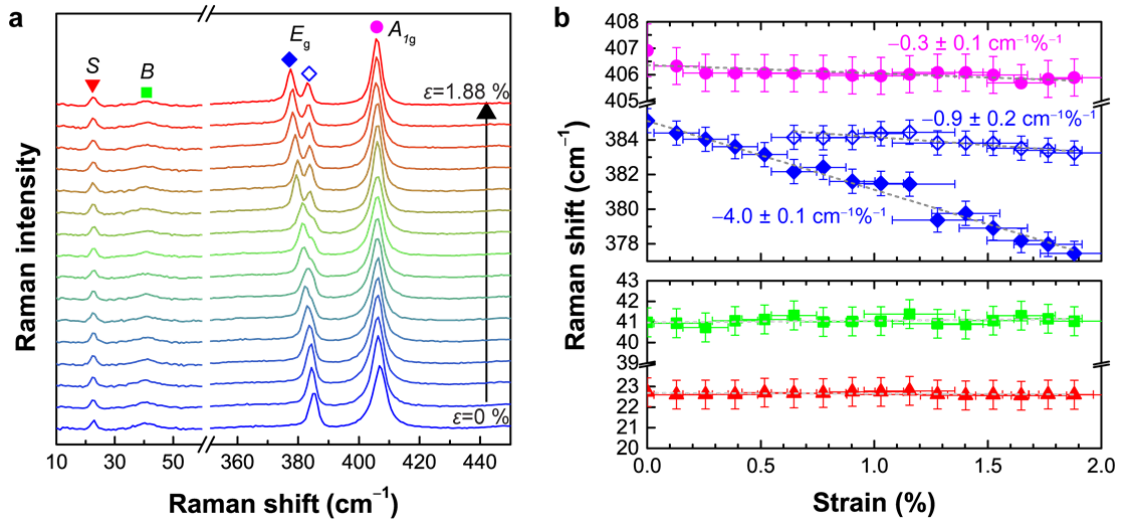


**Figure 3| Raman spectra of bilayer MoS<sub>2</sub> under uniaxial strain.** (a) Raman spectra of bilayer MoS<sub>2</sub> as a function of uniaxial strain. From left to right, the shear, breathing, split E<sub>g</sub>, and A<sub>1g</sub> modes are denoted by the triangle, square, diamond, and circle symbols, respectively. (b) The peak positions for intralayer phonon modes (upper panel) and interlayer shear and breathing modes (lower panel) as a function of uniaxial tensile strain. Error bars in strain come from the uncertainty in the estimate of the strain using the equation  $\epsilon = t_0 \theta / L_0$ . The error bars in Raman shift are defined by spectral resolution of the spectrometer.

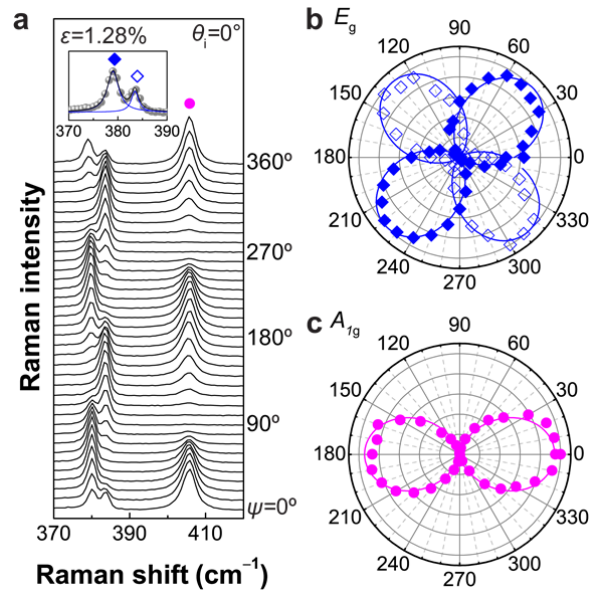


**Figure 4| Polarization dependence of intralayer Raman modes under strain. (a)**

Polarized Raman spectra of strained bilayer MoS<sub>2</sub> (ε=1.28%) for main intralayer modes. The incident polarization ( $\theta$ ) is fixed at 0° and the spectra are measured as a function of  $\psi$  defined in Fig. 1a. Empty and filled diamond and circle symbols are defined in Fig. 3.

Normalized polar plots of (b)  $E_g$  ( $E_g^-$  and  $E_g^+$ ) and (c)  $A_{1g}$  modes.

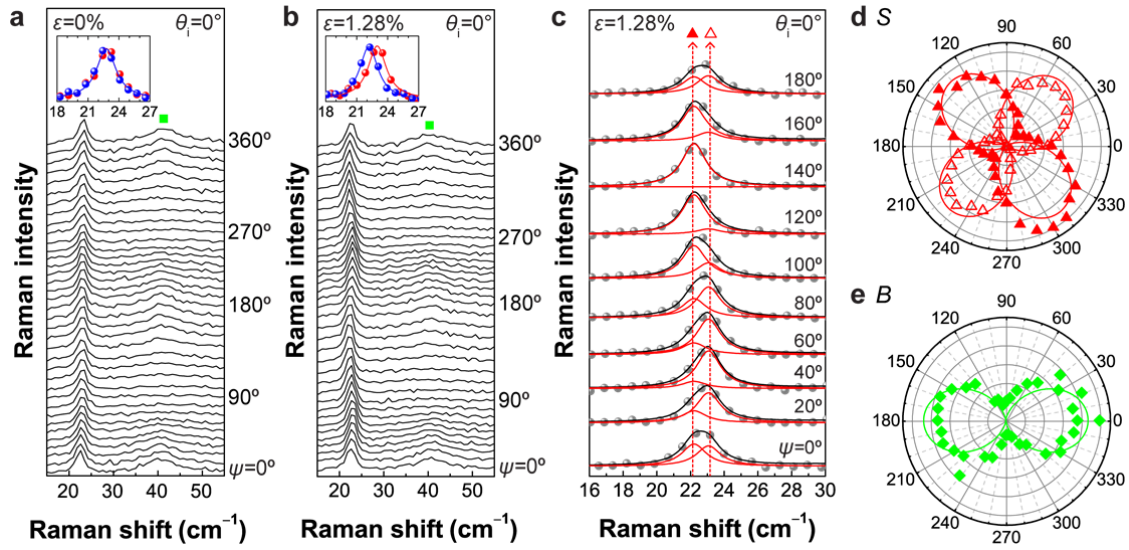


**Figure 5 | Polarization dependence of interlayer Raman modes.** Polarized Raman spectra of bilayer MoS<sub>2</sub> (a) without and (b) with strain ( $\epsilon=1.28\%$ ) in the low-frequency region. The incident polarization ( $\theta_i$ ) is fixed at  $0^\circ$  and the spectra are measured as a function of  $\psi$  defined in Fig. 1a. The insets compare spectra taken for  $\psi=40^\circ$  (blue) and  $130^\circ$  (red) and show the splitting for the case with strain. (c) Representative fitting results for split shear modes. Normalized polar plots of (d) shear ( $S$ ,  $S^-$  and  $S^+$ ) and (e) breathing ( $B$ ) modes.

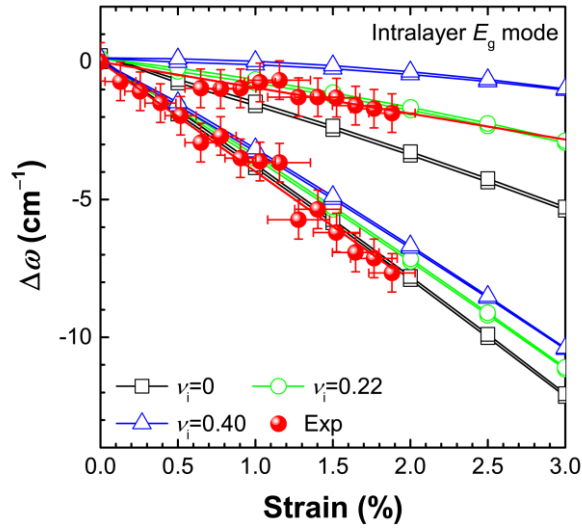


**Table 1| Elastic constants of bilayer MoS<sub>2</sub>.** Summary of elastic constants estimated from experimental results.

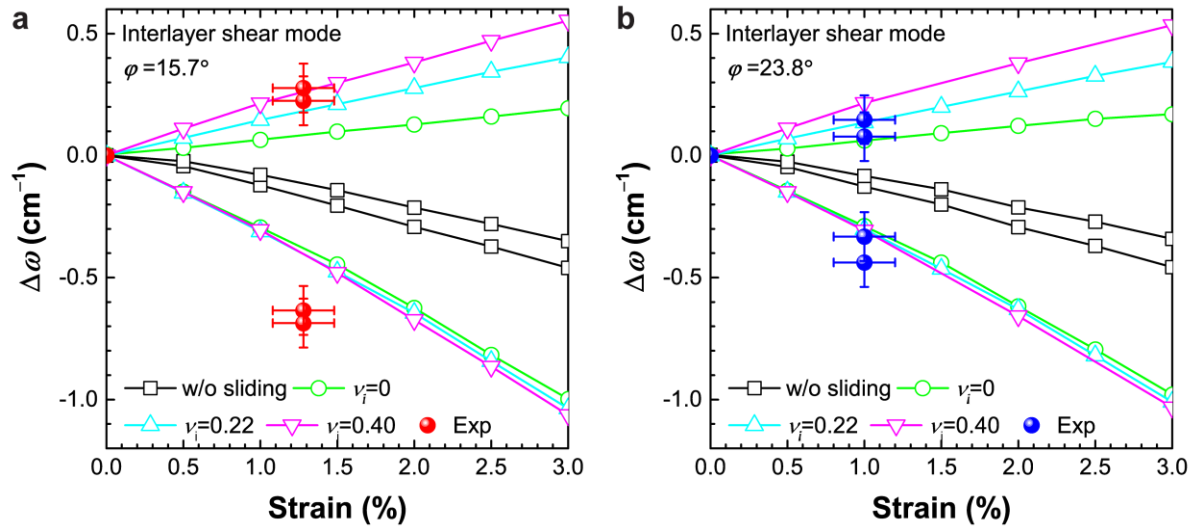
<b>Elastic constants</b>	<b>Value</b>	<b>References</b>
$s_{14}$	$-1.46 \pm 0.34 \text{ TPa}^{-1} \text{ (exp)} / -0.84 \text{ TPa}^{-1} \text{ (cal)}$	This work
$s_{44}$	$111 \pm 8 \text{ TPa}^{-1} \text{ (exp)}^a / 154 \text{ TPa}^{-1} \text{ (cal)}$	This work
$E_i$	$0.33 \text{ TPa (exp)}$	Ref. 36
$E_o$	$0.058 \pm 0.002 \text{ TPa (exp)}^b$	This work
$\nu_i$	$0.22 \text{ (cal)}$	Ref. 33
$\nu_o$	$0.18 \text{ (cal)}$	Ref. 33

<sup>a</sup> Experimental value of  $s_{44}$  was estimated from  $c_{44}$ , obtained from the position of the (unstrained) shear modes<sup>14,15</sup>, assuming that off-diagonal elements are much smaller than diagonal elements ( $s_{44} \approx 1/c_{44}$ ).

<sup>b</sup> Experimental value of  $E_o$  was obtained from the position of the (unstrained) breathing mode<sup>14,15</sup>.



**Supplementary Figure 1| Dependence of shift rates of intralayer  $E_g$  modes on Poisson's ratio.** Comparison of shift rates of intralayer  $E_g$  modes calculated for three different in-plane Poisson's ratio values of 0 (black square), 0.22 (green circle, intrinsic value of  $\text{MoS}_2$ ), and 0.40 (blue triangle, value for acrylic substrate). Experimental results are shown as red symbols. All the results are for  $\varphi = 15.7^\circ$ . Experimental error bars in strain come from the uncertainty in the estimate of the strain from the curvature of the bent substrate. The error bars in  $\Delta\omega$  are defined by the standard deviation of experimental values.

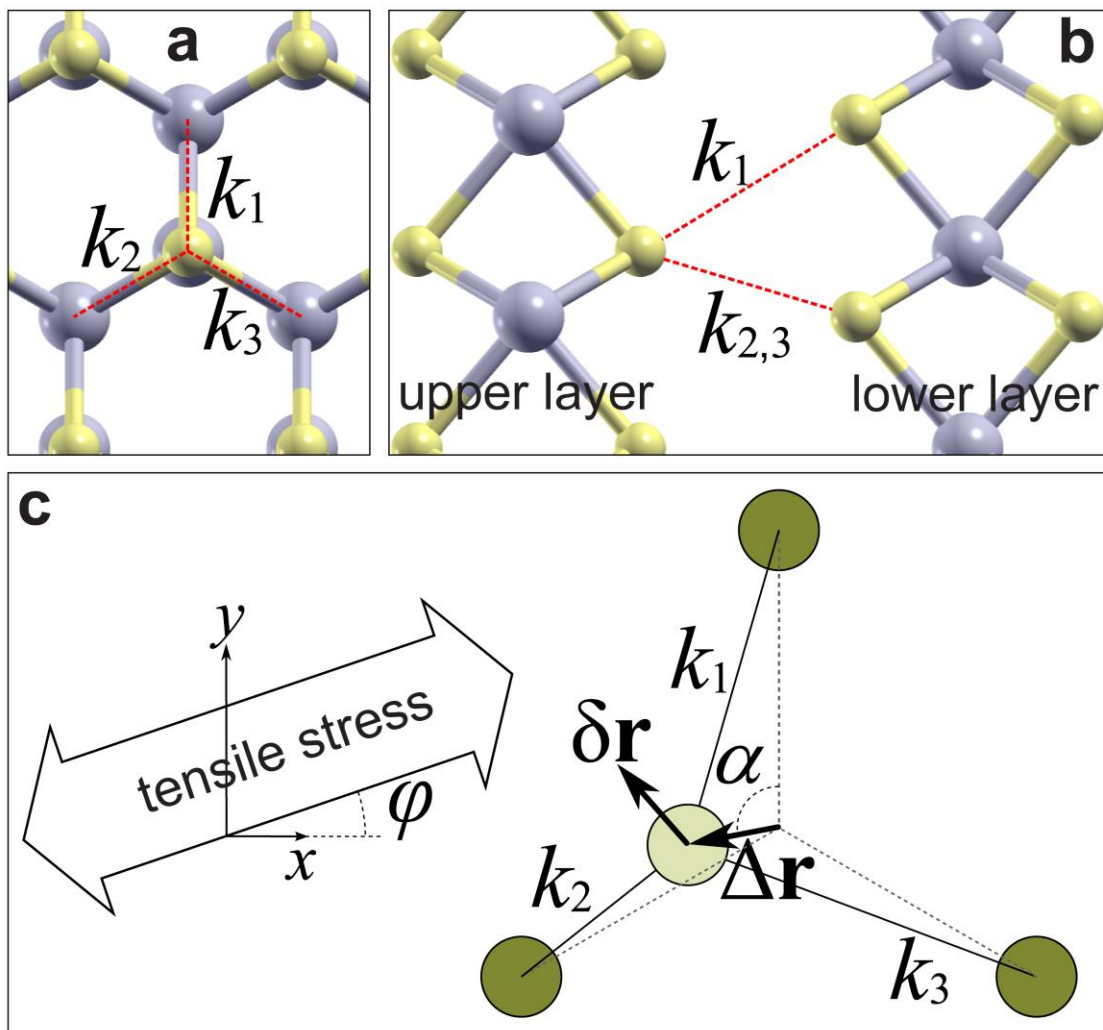


**Supplementary Figure 2| Effect of sliding on peak shift of interlayer shear mode as a function of uniaxial strain.** Calculated peak shifts without including sliding (black square) and with sliding (other open symbols) are shown for **(a)**  $\varphi = 15.7^\circ$  and **(b)**  $\varphi = 23.8^\circ$ . Peak shifts with sliding are estimated for three different Poisson's ratio values of 0 (green circle), 0.22 (cyan triangle, intrinsic value of MoS<sub>2</sub>), and 0.40 (magenta reversed triangle, value for acrylic substrate). Experimental results as filled symbols (red for  $\varphi = 15.7^\circ$  and blue for  $\varphi = 23.8^\circ$ ) are also shown. Experimental error bars in strain come from the uncertainty in the estimate of the strain from the curvature of the bent substrate. The error bars in  $\Delta\omega$  are defined by the standard deviation of experimental values.

### Supplementary Note 1: Calculation of peak splitting based on ball-and-stick model

The frequencies of the interlayer shear phonon modes in the Raman spectrum are determined by the effective interatomic spring constants between bottom sulfur atoms of the upper MoS<sub>2</sub> layer and the top sulfur atoms of the lower layer as in Supplementary Figs. 3a and b.

Supplementary Fig. 3c shows the top view schematically with the sulfur atom from the upper layer having lighter color. The parameters  $k_1$ ,  $k_2$ , and  $k_3$  are the lateral components of



**Supplementary Figure 3| Structure of MoS<sub>2</sub> and definition of parameters.** (a) Top and (b) side view of a relaxed structure of bilayer 2H-MoS<sub>2</sub>.  $k_1$ ,  $k_2$ , and  $k_3$  are indicated. (c) Ball-and-stick model with interlayer sliding.

effective spring constants between one of the sulfur atoms in the upper layer and its three nearest-neighbor sulfur atoms from the lower layer.  $\delta\mathbf{r}$  in Supplementary Fig. 3c is the lateral dynamical displacement vector of an interlayer shear phonon mode from the shifted position  $\Delta\mathbf{r}$ . Let us set the direction of the sliding to be  $\alpha$  from the positive y axis so that  $\alpha = -2\varphi$  for  $s_{14} > 0$  and  $\alpha = \pi - 2\varphi$  for  $s_{14} < 0$ . Here,  $\Delta\mathbf{r}$  and  $\varphi$  are defined in the main text.

The lateral sliding,  $\Delta\mathbf{r}$ , changes the frequency of the interlayer shear mode by modifying the interatomic spring constants,  $k_i$ 's. The interatomic spring constant changes linearly if the sliding is small enough so that  $k_i = k - \gamma'\Delta a_{ss}^i$ , where  $k$  is the spring constant without strain,  $\gamma'$  is a linear scaling factor, and  $\Delta a_{ss}^i = a_{ss}^i - a_{ss}$  is the change of the corresponding nearest-neighbor distance with  $a_{ss}$  being the interatomic distance without strain. Up to the first order of  $|\Delta\mathbf{r}|$ ,  $\Delta a_{ss}^1 \approx -|\Delta\mathbf{r}|\cos\alpha$ ,  $\Delta a_{ss}^2 \approx |\Delta\mathbf{r}|\cos(\frac{\pi}{3} + \alpha)$ , and  $\Delta a_{ss}^3 \approx |\Delta\mathbf{r}|\cos(\frac{\pi}{3} - \alpha)$  so that  $k_1 \approx k + \gamma'|\Delta\mathbf{r}|\cos\alpha$ ,  $k_2 \approx k - \gamma'|\Delta\mathbf{r}|\cos(\frac{\pi}{3} + \alpha)$ , and  $k_3 \approx k - \gamma'|\Delta\mathbf{r}|\cos(\frac{\pi}{3} - \alpha)$ .

A dynamical displacement vector under an excitation of an interlayer shear phonon mode,  $\delta\mathbf{r} = (\delta x, \delta y)$ , changes interatomic distances dynamically from the shifted positions such that  $\delta a_1 = -\delta y$ ,  $\delta a_2 = \frac{\sqrt{3}}{2}\delta x + \frac{1}{2}\delta y$ ,  $\delta a_3 = -\frac{\sqrt{3}}{2}\delta x + \frac{1}{2}\delta y$ . With modified spring constants  $k_i$ 's and corresponding  $\delta a_{ss}^i$ 's, the potential energy is given by  $U = \sum_{i=1}^3 \frac{1}{2}k_i\delta a_i^2$ , which in turn can be expressed in terms of  $\delta\mathbf{r}$  as  $U = \frac{1}{2}\delta\mathbf{r}^T K \delta\mathbf{r}$ , where  $K$  is a  $2 \times 2$  matrix,

$$K = \begin{pmatrix} \frac{3}{2}k - \frac{3}{4}\gamma'|\Delta\mathbf{r}|\cos\alpha & \frac{3}{4}\gamma'|\Delta\mathbf{r}|\sin\alpha \\ \frac{3}{4}\gamma'|\Delta\mathbf{r}|\sin\alpha & \frac{3}{2}k + \frac{3}{4}\gamma'|\Delta\mathbf{r}|\cos\alpha \end{pmatrix}. \quad (1)$$

The eigenvalues,  $k_{\pm} = \frac{3}{2}k \pm \frac{3}{4}\gamma'|\Delta\mathbf{r}| = \frac{3}{2}k \pm \frac{3}{4}d_{\text{int}}|s_{14}|\sigma$ , and eigenvectors,  $\delta\mathbf{r}_{+} = (\sin\frac{\alpha}{2}, \cos\frac{\alpha}{2})$  and  $\delta\mathbf{r}_{-} = (\cos\frac{\alpha}{2}, -\sin\frac{\alpha}{2})$ , of  $K$  represent the effective spring constants and displacement vectors of the corresponding normal modes, respectively.

The vibration directions of the phonon modes,  $\alpha_{\pm}$ , are obtained from  $\tan\alpha_{\pm} = \delta y / \delta x$  and given by  $\alpha_{+} = \pi/2 - \alpha/2$  and  $\alpha_{-} = -\alpha/2$ . Using the relation between  $\alpha$  and  $\varphi$  depending on the sign of  $s_{14}$ ,  $\alpha_{+} = \varphi + \pi/2$  and  $\alpha_{-} = \varphi$  for  $s_{14} > 0$  whereas  $\alpha_{+} = \varphi$  and  $\alpha_{-} = \varphi - \pi/2$  for  $s_{14} < 0$ . Since the reduced mass of interlayer shear modes for a primitive unit cell is  $m_{\text{r}} = (m_{\text{Mo}} + 2m_{\text{S}})/2$ , the phonon frequencies,  $\omega_{\pm} = \sqrt{k_{\pm}/m_{\text{r}}}$ , are

$$\omega_{\pm} \approx \omega_0 \pm \frac{\omega_0 d_{\text{int}} \gamma' |s_{14}| E_i}{4k} \varepsilon, \quad (2)$$

where  $\omega_0 = \sqrt{3k/(m_{\text{Mo}} + 2m_{\text{S}})}$  and  $m_{\text{Mo}}$  and  $m_{\text{S}}$  are the masses of molybdenum and sulfur atoms, respectively. Here, we used  $\varepsilon = \sigma/E_i$  where  $\varepsilon$  is the strain along the applied uniaxial stress  $\sigma$ , and  $E_i$  is the in-plane Young's modulus.

Supplementary Equation (2) reflects only the effect of induced sliding that causes splitting, not the effect of the direct spring constant modification due to the tensile strain which is supposed to shift the average of split frequencies,  $\bar{\omega} = \frac{\omega_{+} + \omega_{-}}{2}$ . In order to estimate  $\bar{\omega}$ , we consider the case of an equibiaxial strain,  $\varepsilon_{\text{eq}}$ , where all the spring constants are scaled as

$k \rightarrow k - \gamma' a_{\text{SS}} \varepsilon_{\text{eq}}$  so that the effective spring constant for the reduced mass system becomes

$\frac{3}{2}k \rightarrow \frac{3}{2}k - \frac{3}{2}\gamma' a_{\text{SS}} \varepsilon_{\text{eq}}$ . The corresponding shift of the average frequency becomes

$\Delta\bar{\omega} = -\frac{\omega_0 \gamma' a_{\text{SS}}}{2k} \varepsilon_{\text{eq}}$ . Using the in-plane Poisson's ratio of the bilayer MoS<sub>2</sub>,  $\nu_i = 0.22$  and

assuming linear response of the sample to the external strain,  $\Delta\bar{\omega}$  for our experiment will become

$$\Delta\bar{\omega} = -\frac{(1-\nu_i)\omega_0\gamma'a_{ss}}{4k}\varepsilon \quad (3)$$

It is worth noting that from Supplementary Equations (2) and (3),  $|s_{14}|$  can be expressed as

$$|s_{14}| = \frac{a_{ss}}{d_{\text{int}}}\frac{(1-\nu_i)}{2E_i}\frac{(\omega_+ - \omega_-)}{\Delta\bar{\omega}}, \quad (4)$$

where  $\omega_+ - \omega_-$  and  $\Delta\bar{\omega}$  can be determined by Raman measurements.

## Supplementary Note 2: First principles calculations of elasticity constants

The shear part of the stiffness tensor of a system with  $D_{3d}$  symmetry in a matrix form can be written by only three independent parameters,

$$\begin{pmatrix} \sigma_4 \\ \sigma_5 \\ \sigma_6 \end{pmatrix} = \begin{pmatrix} c_{44} & 0 & 0 \\ 0 & c_{44} & c_{56} \\ 0 & c_{56} & c_{66} \end{pmatrix} \begin{pmatrix} \varepsilon_4 \\ \varepsilon_5 \\ \varepsilon_6 \end{pmatrix} \quad (5)$$

with the choice of  $z$  as the axis for the three-fold rotational symmetry. The components of stiffness tensor can be obtained by differentiating the total energy  $E_{\text{tot}}$  in terms of shear strain;  $c_{44} = \partial^2 E_{\text{tot}} / \partial \varepsilon_4^2$ ,  $c_{66} = \partial^2 E_{\text{tot}} / \partial \varepsilon_6^2$ , and  $c_{56} = \partial^2 E_{\text{tot}} / \partial \varepsilon_5 \partial \varepsilon_6$ . By taking the inverse of stiffness tensor, one can get the shear part of compliance tensor, Eq. (1) in the main text.

Using a first-principles approach based on density-functional theory with plane wave basis set, we calculate total energies  $E_{\text{tot}}(\varepsilon_4, \varepsilon_5, \varepsilon_6)$ , at  $5 \times 5 \times 5$  grid points in the shear strain space.

For the total energy calculations with tensile strain for a bilayer system, in-plane primitive unit cell vectors  $u_1 = (a, 0, 0)$  and  $u_2 = (b, c, 0)$  are used. The unit cell along the  $z$  axis is set to be larger than 7 nm in order to reduce interactions between supercells. Let us define  $a_0, b_0, c_0$  for the values of  $a, b, c$  for a system without strain, which has relations,  $b_0 = a_0 / 2$  and

$c_0 = \sqrt{3}a_0 / 2$ . For simulating interlayer shear strain, we further define the displacement of the top layer with respect to the bottom layer along the  $x$  and  $y$  directions as  $disp_i$ , where  $i = x, y$ .

Inter- and intra-layer shear strains are defined as  $\varepsilon_4 = 2\varepsilon_{yz} = disp_y / d_{\text{int}}$ ,

$\varepsilon_5 = 2\varepsilon_{xz} = disp_x / d_{\text{int}}$ , and  $\varepsilon_6 = 2\varepsilon_{xy} = (b - b_0) / c_0$ . Here,  $d_{\text{int}}$  is the interlayer distance. The

values for  $c_{44}$ ,  $c_{66}$ , and  $c_{56}$  are calculated by interpolating the total energy in the shear strain grid and so is the compliance tensor.



### Supplementary Note 3: Calculation of Grüneisen parameters

Assuming linear dependence of the frequencies on the uniaxial strain, the shift rates of the  $E_g^-$ ,  $E_g^+$ , and  $A_{1g}$  modes for bilayer MoS<sub>2</sub> are obtained to be  $-4.0 \pm 0.1$ ,  $-0.9 \pm 0.2$ , and  $-0.3 \pm 0.1 \text{ cm}^{-1}\%^{-1}$ , respectively. From the shift rates, the Grüneisen parameter ( $\gamma$ ) and the deformation potential ( $\beta$ ) were calculated for the  $E_g$  mode of bilayer MoS<sub>2</sub> using the following equations<sup>1</sup>.

$$\gamma = \frac{\Delta\omega_+ + \Delta\omega_-}{2\omega_0(1-\nu_i)\varepsilon} \quad \text{and} \quad (6)$$

$$\beta = \frac{\Delta\omega_+ - \Delta\omega_-}{2\omega_0(1+\nu_i)\varepsilon}, \quad (7)$$

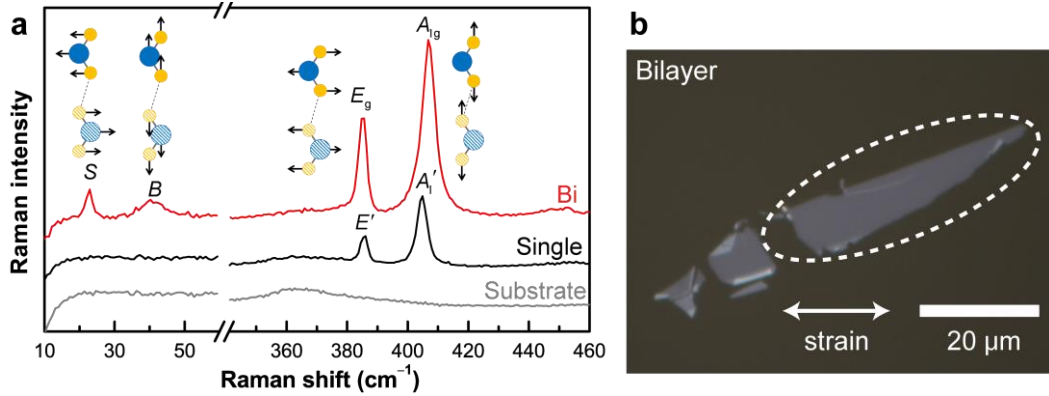
where  $\omega_0$  is the peak position of the  $E_g$  mode without strain,  $\Delta\omega_{+(-)}$  is the peak shift of  $E_g^+$  ( $E_g^-$ ) under strain with respect to  $\omega_0$ ,  $\varepsilon$  is the strain, and  $\nu_i$  is the in-plane Poisson's ratio of MoS<sub>2</sub>. We used the Poisson's ratio of 0.22<sup>2</sup>. The obtained parameters are  $\gamma = 1.0 \pm 0.2$  and  $\beta = 0.8 \pm 0.2$  for the  $E_g$  mode. We applied the same method to the interlayer shear ( $S$ ) mode and obtained  $\gamma = 0.9 \pm 0.3$  and  $\beta = 2.4 \pm 0.4$ .

#### Supplementary Note 4: Determination of crystallographic orientation

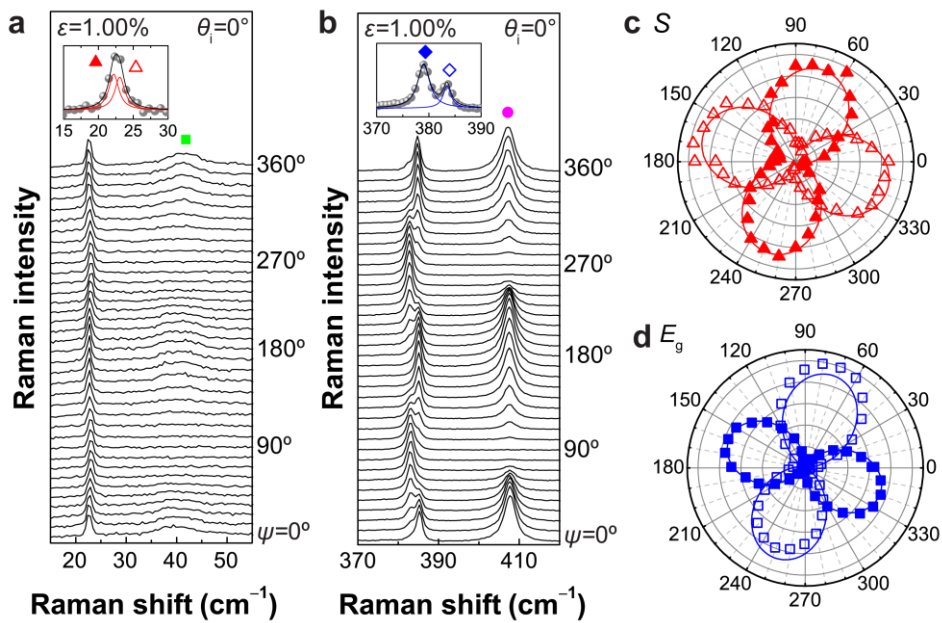
For the  $E_g^-$  mode, the atomic displacement is parallel to strain axis, whereas the  $E_g^+$  mode is perpendicular to it. By considering a linear combination of the two modes, one can obtain the polarization dependence of  $E_g^-$  and  $E_g^+$  modes as follows<sup>1</sup>.

$$I_{E_g^-} \propto \sin^2(\theta_i + \theta_s - 3\varphi) \quad \text{and} \quad I_{E_g^+} \propto \cos^2(\theta_i + \theta_s - 3\varphi), \quad (8)$$

where  $\theta_i$  is an angle between the incident polarization and the strain direction,  $\theta_s$  is an angle between the scattered polarization and the strain direction, and  $\varphi$  is an angle between the strain direction and the zigzag direction as shown in Fig. 1a. By fitting the experimental data with the above equations, we obtained the crystallographic orientation of the samples with respect to the zigzag direction.



**Supplementary Figure 4| Raman spectra and optical image of samples. (a)** Raman spectra of single and bilayer MoS<sub>2</sub> on acrylic substrate. **(b)** Optical image of bilayer sample.



**Supplementary Figure 5| Polarization dependence of Raman modes for an additional sample.** Polarized Raman spectra of strained bilayer MoS<sub>2</sub> ( $\varepsilon = 1.00\%$ ) for **(a)** inter- and **(b)** intra-layer modes. The incident polarization ( $\theta_i$ ) is fixed at  $0^\circ$  and the spectra are measured as a function of  $\psi$  defined in Fig. 1a. Symbols are defined in Fig. 2. Normalized polar plots of **(c)**  $E_g$  ( $E_g^-$  and  $E_g^+$ ) and **(d)** shear ( $S$ ,  $S^-$  and  $S^+$ ) modes.

## Supplementary References

1. Mohiuddin, T. M. G. *et al.* Uniaxial strain in graphene by Raman spectroscopy: *G* peak splitting, Grüneisen parameters, and sample orientation. *Phys. Rev. B* **79**, 205433 (2009).
2. Woo, S., Park, H. C. & Son, Y.-W. Poisson's ratio in layered two-dimensional crystals. *Phys. Rev. B* **93**, 75420 (2016).